ISSN 1392-1207. MECHANIKA. Vol. 32, No. 1, 2026: 20–28

Influence of Pressure Angle on the Dynamic Characteristics of Asymmetric Helical Gear Transmissions

Xue-zhong FU*, Jian-shu MAN, Jun ZOU***, Shu-ping LI******

**School of Mechanical and Automotive Engineering, Guangxi University of Science and Technology, Liuzhou 545006, China; E-mail: 100002350@gxust.edu.cn*

***School of Mechanical and Automotive Engineering, Guangxi University of Science and Technology, Liuzhou 545006, China; E-mail: 20230103049@stdmail.gxust.edu.cn*

****Technical Center of Fangsheng Axle (Liuzhou) Co., Ltd., Liuzhou 545616, China; E-mail: zoujun@fangshengaxle.com*

*****School of Mechanical and Automotive Engineering, Guangxi University of Science and Technology, Liuzhou 545006, China; E-mail: 100001550@gxust.edu.cn (Corresponding Author)*

https://doi.org/10.5755/j02.mech.43041

1 Introduction

Asymmetric helical gears employ distinct pressure angles on the driving and coast sides of the tooth profile, offering higher load capacity, reduced weight, and longer service life than symmetric designs [1, 2]. This performance gain stems from pressure angle asymmetry, which reshapes tooth geometry and stress distribution, thereby critically influencing system dynamics.

Regarding fundamental design and static strength, foundational work by Litvin et al. [3] established the principle of using a larger pressure angle on the driving side to optimize contact and reduce stresses. Kapelevich's numerical study [4] confirmed the potential of asymmetric design to enhance load capacity, reduce weight, and vibration. Xiao et al. [5-7] systematically investigated the design methods, tooth profile modeling, and meshing simulations of asymmetric gears, developing analytical and finite element approaches for evaluating root bending and contact stresses. Importantly, the effect of pressure angle asymmetry on fatigue performance has been experimentally validated. A moderate increase can improve bending fatigue life by approximately 90% and alter failure modes, highlighting its profound impact on stress redistribution [8]. Additionally, optimizing the tooth root geometry, such as using a circular fillet, effectively enhances root strength and fatigue life [9]. These findings confirm that pressure angle is a key design parameter for optimizing both static and fatigue performance.

The transition from static to dynamic performance introduces core dynamic excitations, primarily time-varying meshing stiffness and meshing impact. Zhu [10] established a tooth profile model of asymmetric gears through ADAMS-based virtual prototype simulation. Marafona et al. [11] pointed out that the asymmetry of tooth geometry significantly alters the frequency components of meshing stiffness, thereby affecting the vibration response and stability of the gear system. Donmez et al. [12] developed a torsional dynamic model for electric drive systems to analyze the effects of time-varying meshing stiffness, backlash, tooth profile errors, and motor torque fluctuations on system vibrations, transient responses, and meshing forces. Mo et al. [13, 14] derived a time-varying meshing stiffness model for asymmetric helical gears using the potential energy method and the slicing method, considering the influence of adjacent teeth on gear body deformation, and further clarified the effects of geometric parameters and tooth modifications on meshing stiffness, transmission error, and load distribution. Li et al. [15] compared the vibration characteristics and time-varying meshing stiffness under different pressure angles and proposed methods to optimize stiffness distribution. Yang et al. [16] established both a numerical model for time-varying meshing stiffness and a six-degree-of-freedom friction–dynamic model for double-pressure-angle asymmetric involute gears, and analyzed dynamic behavior by introducing variable pressure angles. Chen et al. [17] incorporated time-varying meshing stiffness and backlash into the dynamic model of asymmetric gears and examined the nonlinear dependence of dynamic performance on average meshing stiffness. Li [18] developed a dynamic model for double-pressure-angle asymmetric gears, taking into account nonlinear tooth contact, angular contact, axial effects, and time-varying meshing stiffness, and proposed a phase configuration method for idler and multistage gear systems. For meshing impact mechanisms, Wang [19] developed a full-tooth-meshing-period impact model considering the effects of nonuniform base pitch errors on the engagement impact at the meshing-in position.

Although previous studies have discussed the dynamic characteristics of asymmetric helical gears to some extent, the effects of time-varying meshing stiffness and meshing impact variations are often neglected, and systematic investigations under different pressure angles are lacking. To gain deeper insight into the dynamic performance of asymmetric helical gears, this study establishes a dynamic model incorporating time-varying meshing stiffness and meshing impact, and explores the influence of pressure angle parameters on system responses. This provides a theoretical foundation for improving dynamic performance and broadening the application scope of asymmetric helical gears.

2. Calculation of Time-Varying Meshing Stiffness and Meshing Impact

During gear operation, single-tooth and double-tooth meshing alternate periodically, causing the meshing stiffness of the gear pair to vary periodically. Moreover, the stiffness values differ at various meshing positions. Based on the meshing stiffness calculation principles described in Refs. [20, 21], the geometric transmission error T_G of the

asymmetric helical gear pair is first obtained through geometric contact analysis. Then, its loaded transmission error T_L is obtained via loaded tooth contact analysis (LTCA) based on a three-dimensional finite element model. This finite element model is built according to the design parameters in Table 2; consequently, the tooth root thickening effect resulting from the increased pressure angle on the driving side is inherently included in the geometry, allowing the LTCA to accurately reflect the root region's resistance to deformation. Accordingly, the total normal deformation of the helical gear pair at any instant is denoted as δ_T and can be determined by Eq. (1):

$$\delta_T = \frac{\pi \left| T_G - T_L \right| r_b}{3600 \times 180}, \tag{1}$$

where: r_b is the base circle radius.

Assume that there are eight meshing positions for a single pair of teeth within one meshing period T, and a total of N meshing positions from engagement to disengagement. The single-tooth meshing stiffness and total meshing stiffness at these discrete positions are calculated from the aforementioned LTCA results as:

$$K_{s(j)} = K_m L_k \left(j = 1, 2, \cdots, N \right), \tag{2}$$

$$K_{m(i)} = \frac{F_n}{\delta_{T(i)}} \left(i = 1, 2, ..., 8 \right), \tag{3}$$

where: $K_{s(j)}$ is the single-tooth meshing stiffness, K_m is the mesh stiffness per unit face width, $K_{m(i)}$ is the total meshing stiffness, L_K is the load distribution factor, F_n is the meshing force.

The meshing stiffness calculated by Eq. (3) is discrete within a meshing period. A polynomial fitting and Fourier series expansion are performed to express it as a periodic function, with the period corresponding to that of the engaged tooth pair. The influence of higher-order Fourier terms is negligible and can be omitted in calculations, thereby obtaining the periodically varying meshing stiffness of the helical gear pair.

Due to tooth deflection under load and manufacturing errors, meshing starts outside the theoretical line of action, resulting in impact at the meshing-in and meshing-out positions, known as meshing impact. Previous studies have shown that the meshing-in impact dominates over the meshing-out impact [22], therefore, this study focuses on the meshing-in impact. Determining the meshing-in impact point requires accurate calculation of the influence of tooth errors and elastic deformation on the equivalent base circle radius. For asymmetric helical gears, multiple pairs of teeth are simultaneously in contact, and tooth deformation plays a significant role. Based on the analysis by Jia et al. [23], the combined normal deformation of multiple engaged tooth pairs is calculated to determine the starting point of the offline meshing-in impact, while considering the contact ratio of the helical gear pair. The meshing-in impact model is established, as illustrated in Fig. 1. In this schematic, K_s and K_q represent the axial support stiffness and radial support stiffness of the gear system, respectively.

This model provides the basis for analyzing the impact behavior during the gear meshing-in process. The meshing-in impact force is then calculated based on impact dynamics, as follows.

The instantaneous rotational inertias of the driving and driven gears, I_1 and I_2, are calculated and transformed into the equivalent masses along the line of action, denoted as m_{red1} and m'_{red2} for the pinion and gear respectively, as follows:

$$\begin{cases} I_1 = \dfrac{\pi \rho b}{2} \left(r_{b1}^4 - r_{h1}^4 \right) \\ I_2 = \dfrac{\pi \rho b}{2} \left(r_{b2}^{'4} - r_{h2}^4 \right) \\ m_{red1} = \dfrac{I_1}{r_{b1}^2} \\ m'_{red2} = \dfrac{I_2}{r_{b2}^{'2}} \end{cases}, \tag{4}$$

where: b is the tooth width, ρ is the gear material density, and r_{h1}, r_{h2} are the inner hub radii of the two gears. The impact kinetic energy at the meshing-in point is given by:

$$E_k = \frac{1}{2} \cdot \frac{m_{red1} m'_{red2}}{\left(m_{red1} + m'_{red2} \right)} v_s^2 = \frac{1}{2} \cdot \frac{I_1 I_2}{\left(I_1 r_{b2}^{'2} + I_2 r_{b1}^2 \right)} v_s^2, \tag{5}$$

where: v_s is the meshing-in impact velocity.

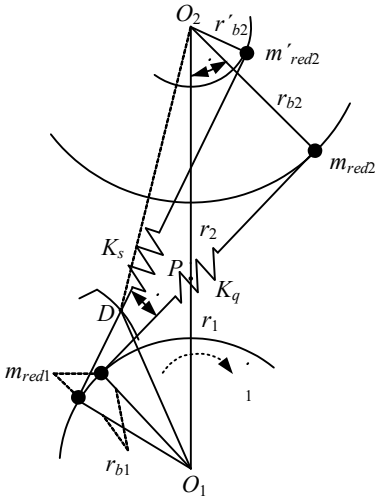

Fig. 1 Schematic diagram of meshing impact

The impact causes an additional deformation δ_s between the gear teeth, and the corresponding maximum impact force is denoted as F_s. According to impact mechanics theory, the relationship among the physical quantities E_k, δ_s, and F_s is given by the following equation:

$$\begin{cases} E_k = \dfrac{1}{2} \cdot \dfrac{I_1 I_2}{\left(I_1 r_{b2}^{'2} + I_2 r_{b1}^2 \right)} v_s^2 = \dfrac{1}{2q_s} \delta_s^{\,2} + \dfrac{1}{2q_q} \delta_q^{\,2} \\ \delta_s = F_s q_s \\ \delta_q = F_s \cos\theta \cdot q_q \end{cases}, \tag{6}$$

$$\theta = \arccos\left(\frac{r'_{b2}}{r_{O_2 D}} \right) - \angle PO_2 D - \alpha, \tag{7}$$

where q_s represents the single-tooth pair flexibility at the initial off-line meshing-in point D, which is obtained by multiplying the total meshing compliance by the load distribution factor; q_q denotes the composite flexibility of the other tooth pairs at the meshing-in moment, excluding the impacted tooth pair, and can be calculated from the total meshing flexibility of all engaged tooth pairs at that instant, as expressed below:

$$\frac{1}{q}=\frac{1}{q_s}+\frac{1}{q_q}. \tag{8}$$

Finally, the meshing-in impact force at the initial impact point is derived as:

$$F_s=v_s\sqrt{\frac{I_1I_2}{\left(I_1r_{b2}^{'2}+I_2r_{b1}^2\right)\left(q_s+cos^2\,\theta\cdot q_p\right)}}. \tag{9}$$

3. Dynamic Modeling of Asymmetric Helical Gear Transmission

Based on the meshing force characteristics of asymmetric helical gears, an eight-degree-of-freedom (8-DOF) dynamic model is established, as shown in Fig. 2. The model includes six translational degrees of freedom and two rotational degrees of freedom.

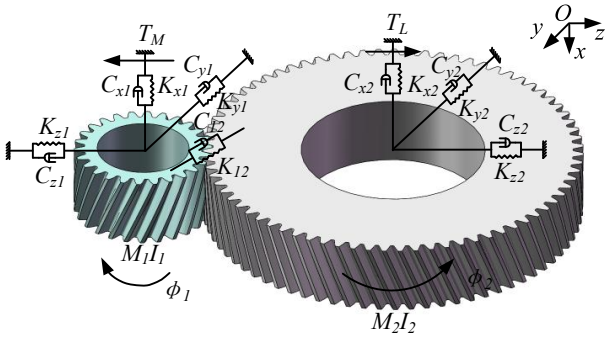

Fig. 2 Dynamic model

The generalized displacement vector U of the system can be expressed as:

$$\vec{U}=\left[x_1,y_1,z_1,\varphi_1,x_2,y_2,z_2,\varphi_2\right], \tag{10}$$

where: x_i, y_i, and z_i (i=1, 2) denote the translational displacements of the driving gear 1 and driven gear 2 in the x, y, and z directions, respectively.

Let Δx_i, Δy_i, and Δz_i represent the installation errors of gear i along the x, y, and z directions, respectively. The relative displacement along the line of action between the gear pair caused by vibration and installation errors is denoted by δ_{12} and is given by:

$$\begin{aligned}\delta_{12}=&\left(\varphi_1r_{b1}-\varphi_2r_{b2}\right)cos\,\beta-\\&-(y_1-y_2+\Delta y_1-\Delta y_2)\,sin\,\zeta\,cos\,\beta-\\&-(z_1-z_2+\Delta z_1-\Delta z_2)\,cos\,\zeta\,cos\,\beta-\\&-\left(x_1-x_2+\Delta x_1-\Delta x_2\right)sin\,\beta,\end{aligned} \tag{11}$$

where: r_{b1} and r_{b2} are the base circle radii of gears 1 and 2, respectively; ζ denotes the angle between the line of action and the positive axis direction; and β represents the helix angle of the helical gear pair.

Based on the 8-DOF dynamic model, the meshing impact effect is incorporated into the modeling process. During system dynamic modeling, the impact is treated as an additional nonlinear force component acting along the line of action, which, together with the time-varying meshing stiffness, constitutes the actual meshing force of the gear pair.

Using the lumped-parameter method, the equations of motion are established, and the dynamic model equations for the driving and driven gears are given by Eqs. (12) and (13), respectively:

$$\begin{cases}M_1\ddot{x}_1+C_{x1}\dot{x}_1+K_{x1}x_1=F_m\,sin\,\beta\\M_1\ddot{y}_1+C_{y1}\dot{y}_1+K_{y1}y_1=F_m\,cos\,\beta\,sin\,\zeta\\M_1\ddot{z}_1+C_{z1}\dot{z}_1+K_{z1}z_1=F_m\,cos\,\beta\,cos\,\zeta\\I_1\ddot{\varphi}_1=T_M-F_m\,cos\,\beta r_{b1}-F_sr_{b1}\end{cases}, \tag{12}$$

$$\begin{cases}M_2\ddot{x}_2+C_{x2}\dot{x}_2+K_{x2}x_2=-F_m\,sin\,\beta\\M_2\ddot{y}_2+C_{y2}\dot{y}_2+K_{y2}y_2=-F_m\,cos\,\beta\,sin\,\zeta\\M_2\ddot{z}_2+C_{z2}\dot{z}_2+K_{z2}z_2=-F_m\,cos\,\beta\,cos\,\zeta\\I_2\ddot{\varphi}_2=F_m\,cos\,\beta r_{b2}-T_L+F_sr_{b2}\end{cases}, \tag{13}$$

where: M_1 and M_2 are the masses of the driving and driven gears, respectively; K_{ji} denotes the stiffness coefficient of gear i(i = 1, 2) along the *j-axis*(j = x, y, z); x_i, y_i, and z_i are the displacements of gear i in the x, y and z directions, respectively; F_m is the meshing force; β is the normal pressure angle; F_s is the meshing-in impact force; M_i is the equivalent lumped mass of gear i; T_M, T_L are the input and output torques of the system, respectively; φ_i denotes the torsional degree of freedom of each component about its own axis.

C_{ji} represents the damping coefficient of gear i along the *j-axis*, and its value is calculated according to Eq. (14).

$$C_{ji}=2\xi_{12}\sqrt{\frac{K_{12}}{\frac{1}{m_{red1}}+\frac{1}{m_{red2}^{'}}}}, \tag{14}$$

where: K_{12} is the mean time-varying comprehensive meshing stiffness of gear pair; ξ_{12} is the meshing damping ratio, taken as 0.1 in this study.

The support stiffness parameters in Eqs. (12) and (13) are crucial for the dynamic simulation. Based on the typical support stiffness ranges in gear systems [24], the following baseline values are adopted in this study and summarized in Table 1.

Table 1

System support stiffness parameters

Parameter	Stiffness value, N/m
Pinion radial support stiffness, K_{x1}, K_{y1}	1.831×10^9
Pinion axial support stiffness, K_{z1}	3.662×10^8
Gear radial support stiffness, K_{x2}, K_{y2}	2.458×10^9
Gear axial support stiffness, K_{z2}	4.085×10^8

The system equations contain rigid-body displacement components. Since rigid-body displacements do not affect the relative motion of the gear pair, retaining them would lead to redundancy in the model formulation. To facilitate analysis, these rigid-body displacement components are eliminated from the system equations. The detailed derivation procedure can be found in Ref. [25].

For subsequent analysis and computation, a reference time scale w_n and a reference displacement scale b_c are introduced to nondimensionalize the system. After eliminating the rigid-body displacements, a seven-degree-of-freedom (7-DOF) dimensionless dynamic equation of motion is obtained, which can be expressed in matrix form as follows:

$$\ddot{\boldsymbol{X}} + \boldsymbol{C}\dot{\boldsymbol{X}} + \boldsymbol{K}\boldsymbol{X} = \boldsymbol{F} \ , \tag{15}$$

where: $\boldsymbol{X}$ is the 7-dimensional dimensionless displacement vector; $\boldsymbol{C}$ is the 7-dimensional dimensionless damping matrix; $\boldsymbol{K}$ is the 7-dimensional dimensionless stiffness matrix; and $\boldsymbol{F}$ is the 7-dimensional dimensionless excitation vector.

4. Case Study

A pair of asymmetric helical gears and a pair of symmetric helical gears are selected for comparative analysis. The two gear pairs share identical basic geometrical parameters, including the number of teeth, normal module, helix angle, face width, addendum coefficient, and clearance coefficient. The only difference lies in the pressure angles on the driving and coast sides, ensuring that the comparison accurately reflects the effect of tooth profile asymmetry on dynamic characteristics. The main parameters are listed in Table 2.

Based on the developed dynamic model, the time-varying meshing stiffness of both gear pairs is calculated under identical operating conditions using LTCA. The results are shown in Fig. 3.

The results indicate that both gear pairs exhibit periodic variations of meshing stiffness within one meshing cycle. However, the asymmetric helical gear pair exhibits a higher average meshing stiffness and smoother stiffness variation compared with the symmetric gear pair. The stiffness trend obtained from LTCA aligns well with the findings reported by Feng et al. [26] for symmetric gears with similar parameters, which were derived using an improved analytical method and validated by finite element analysis. Although the research methodologies differ, both confirm similar stiffness variation characteristics and underlying rules, providing cross-validation for the reliability of the present stiffness results. This can be attributed to the increased tooth thickness on the driving side enhances the load-carrying capacity and stiffness. The corresponding geometric contact ratios for the studied pressure angles are summarized in Table 3, providing insight into the load-sharing characteristics.

Table 2

Comparison of gear parameters

Parameter	Asymmetric helical gear	Symmetric helical gear
Number of teeth Z_1	26	
Number of teeth Z_2	75	
Normal module Mn/(mm)	2	
Pressure angle on driving side α_d/(°)	25	20
Pressure angle on coast side α_c/(°)	20	20
Helix angle β/(°)	21.5	
Face width b/(mm)	30	
Addendum coefficient ha^*	1	
Clearance coefficient c^*	0.25	
Poisson's ratio v	0.3	
Rotational speed n/(r·min^{-1})	10000	

Table 3

Contact ratios under different driving-side pressure angles

Pressure angle on driving side, α_d/(°)	Total contact ratio	Transverse contact ratio
20	3.300	1.550
25	3.122	1.371
30	2.895	1.145
35	2.697	0.947
40	2.522	0.772

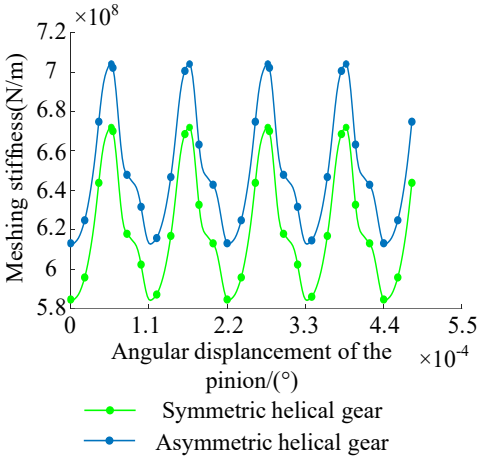

Fig. 3 Time-varying meshing stiffness of symmetric and asymmetric helical gears

The dynamic responses of the two gear pairs are shown in Figs. 4 and 5, including time histories, phase portraits, and Poincaré maps. In the entire paper, the displacement and velocity in the time histories, phase portraits, and Poincaré maps are all taken along the direction of the meshing line. Overall, the asymmetric helical gear exhibits smaller vibration amplitudes, more stable responses, and more concentrated spectral distributions than the symmetric gear, demonstrating superior dynamic stability.

To further investigate the effect of pressure angle on dynamic behavior, different driving-side pressure angles of 25°, 30°, 35°, and 40° are selected for comparison. Their corresponding time-varying meshing stiffness curves are calculated, and their effects on the time histories, phase portraits, and Poincaré maps are analyzed. The results are shown in Figs. 6-9.

As shown in Fig. 6, as the driving-side pressure angle increases from 25° to 40°, the overall level of time-varying meshing stiffness increases, accompanied by larger fluctuation amplitudes. Specifically, the average stiffness increases from 7.13×10^8 to 9.41×10^8 as the pressure angle goes from 25° to 40°. At 40°, the stiffness curve exhibits the highest average value but also stronger oscillations. This indicates that larger pressure angles enhance meshing stiffness

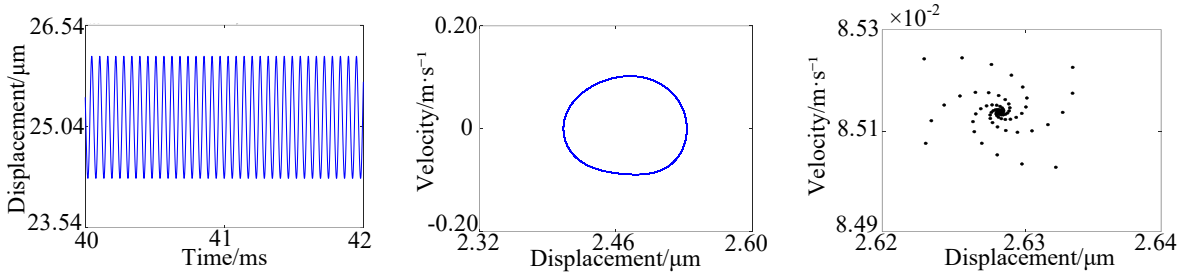

a b c

Fig. 4 Dynamic characteristics of symmetric helical gear: a – time history, b – phase portrait, c – Poincaré map

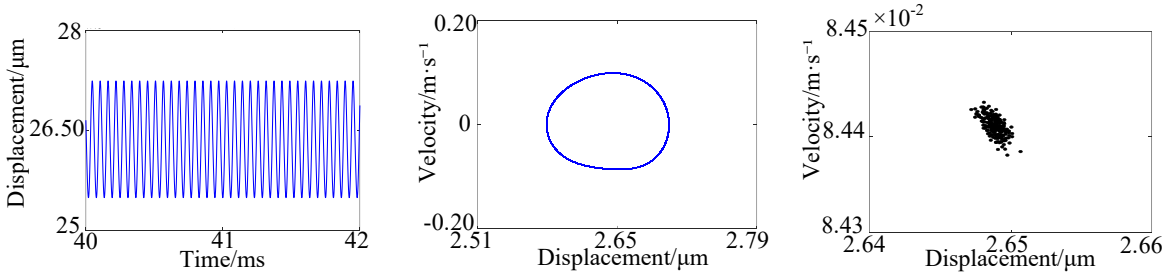

a b c

Fig. 5 Dynamic characteristics of asymmetric helical gear: a – time history, b – phase portrait, c – Poincaré map

but also introduce greater fluctuation intensity. Geometrically, this intensified fluctuation correlates with the decreasing transverse contact ratio, which reduces the number of tooth pairs sharing the load simultaneously.

From a dynamic response perspective, the time histories, phase portraits, and Poincaré maps show clear differences under various driving-side pressure angles. At 25°, the vibration amplitudes are relatively large, and the overall performance is moderate. At 30°, the phase portrait becomes more concentrated, and the response stabilizes. As the pressure angle increases from 30° to 35°, the displacement fluctuation range decreases from approximately 0.81 μm to 0.58 μm, and the displacement spread in the Poincaré map narrows from 5×10^{-3} μm to 2×10^{-3} μm, indicating improved stability. At 35°, the distribution of points in the Poincaré map is the most compact, reflecting optimal periodicity. When the pressure angle further increases to 40°, the displacement fluctuation amplitude in the time-history plot rises to 1.02 μm, and the Poincaré distribution becomes scattered again, with the displacement span returning to 0.01 μm, indicating a reduction in system stability.

To investigate the specific influence of meshing impact on the system's dynamic response, the dynamic loads under different driving-side pressure angles are calculated, as shown in Fig. 10. Under meshing impact, the dynamic loads exhibit periodic pulse characteristics with distinct convex peaks in each meshing cycle.

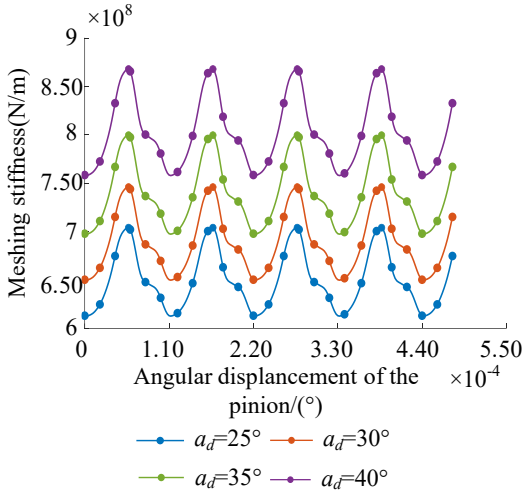

Fig. 6 Time-varying meshing stiffness curves for different driving-side pressure angles

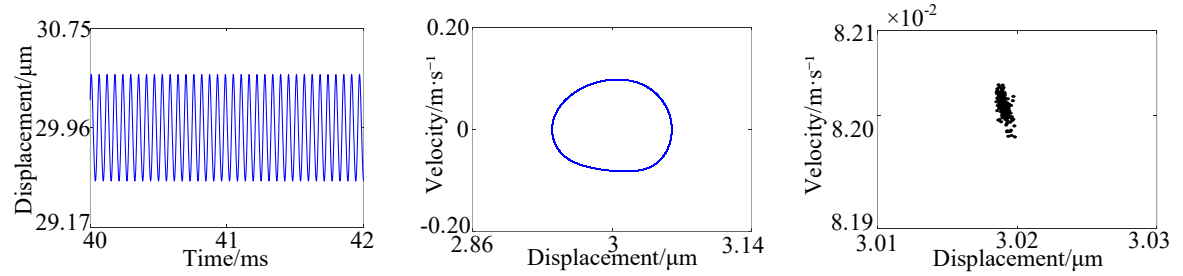

a b c

Fig. 7 Driving-side pressure angle 30°: a – time history, b – phase portrait, c – Poincaré map

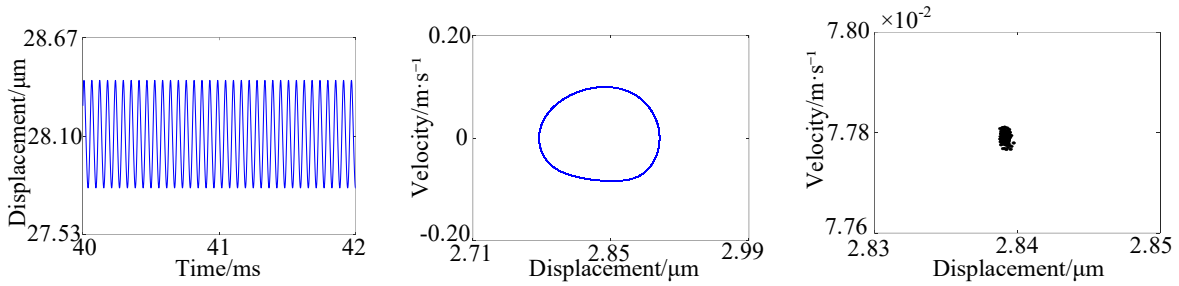

a b c

Fig. 8 Driving-side pressure angle 35°: a – time history, b – phase portrait, c – Poincaré map

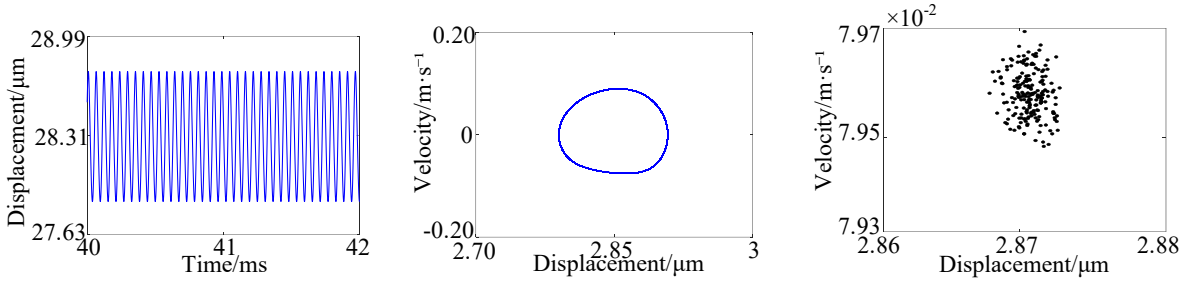

a b c

Fig. 9 Driving-side pressure angle 40°: a – time history, b – phase portrait, c – Poincaré map

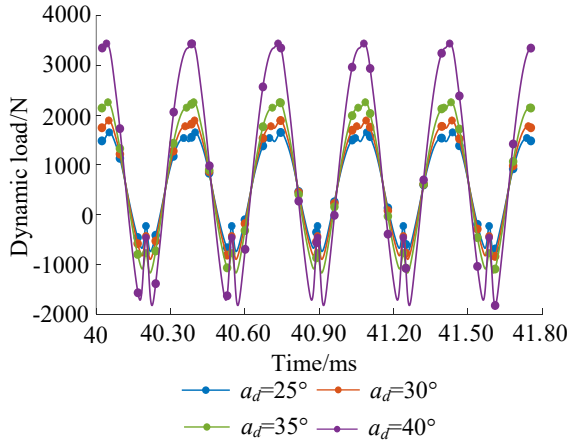

Fig. 10 Dynamic load under different driving-side pressure angles

At 25°, the pronounced load fluctuations indicate reduced system stability. When the pressure angle increases to 30° and 35°, the impact amplitude is effectively suppressed, with the peak meshing impact decreasing from approximately 713.41 N to 537.22 N, resulting in a smoother load curve and improved stability. At 40°, although the average meshing stiffness increases, the impact intensifies, with the peak impact load sharply rising to nearly 1481.67 N, leading to larger load peaks and reduced overall stability.

On this basis, to further compare the effects of meshing impact on the system response characteristics under different pressure angles, the time histories, phase portraits, and Poincaré maps corresponding to the 25°, 30°, 35°, and 40° conditions are presented in Figs. 11-14.

These results indicate that under meshing impact, the system's dynamic responses vary significantly with the driving-side pressure angle. At 25°, the displacement time-history vibration amplitude is about 2.50 μm and the Poincaré section displacement is 0.04 μm, showing a dispersed distribution and poor stability. As the pressure angle increases to 30° and 35°, average meshing stiffness rises, fluctuations between single- and multi-tooth meshing stages become more balanced, and the vibration amplitude decreases by 27.20% and 13.60% to 1.85 μm and 2.16 μm, with the Poincaré section displacement also reducing. Meanwhile, peak meshing impacts diminish, and response curves smooth out, with phase trajectories forming regular closed loops indicative of low-period or quasi-periodic behavior.

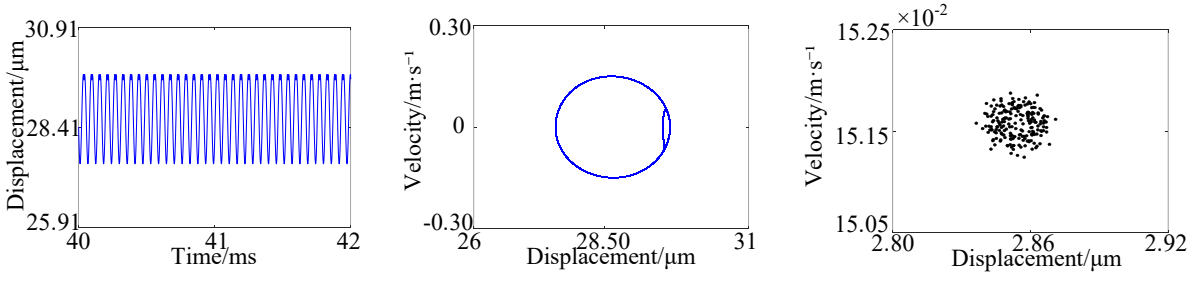

a b c

Fig. 11 Meshing impact at a driving-side pressure angle of 25°: a – time history, b – phase portrait, c – Poincaré map

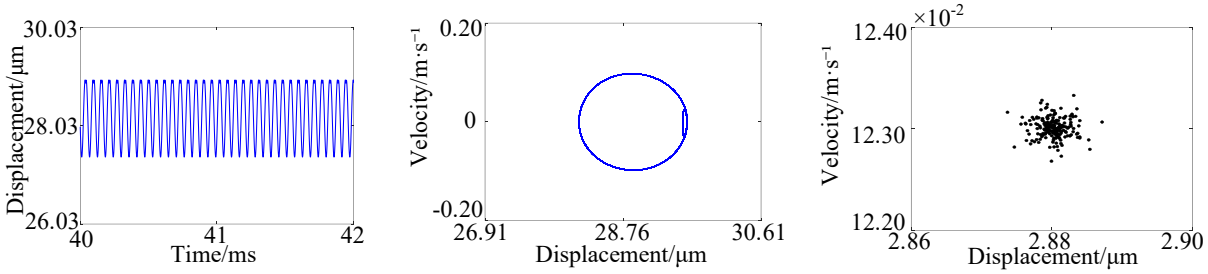

a b c

Fig. 12 Meshing impact at a driving-side pressure angle of 30°: a – time history, b – phase portrait, c – Poincaré map

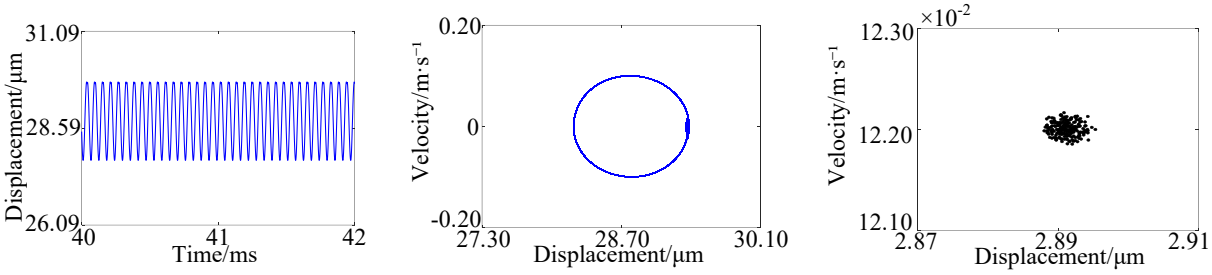

a b c

Fig. 13 Meshing impact at a driving-side pressure angle of 35°: a – time history, b – phase portrait, c – Poincaré map

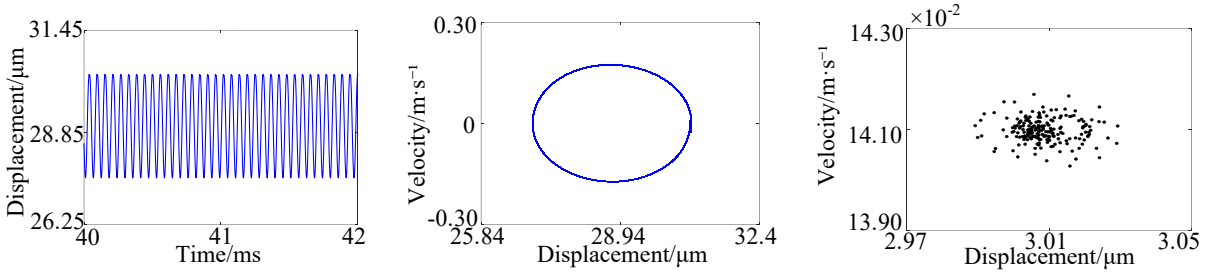

a b c

Fig. 14 Meshing impact at a driving-side pressure angle of 40°: a – time history, b – phase portrait, c – Poincaré map

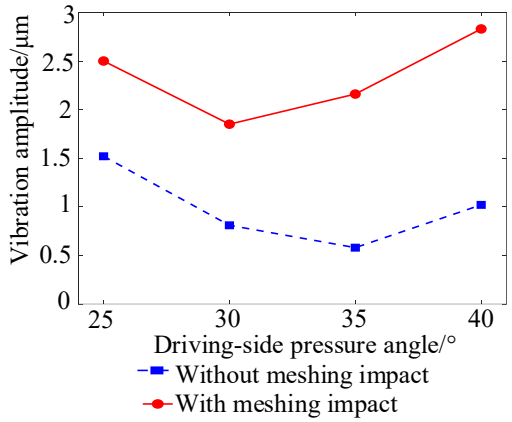

Fig. 15 Comparison of vibration amplitudes with and without meshing impact

At 40°, although average stiffness continues to grow, variations in meshing geometry and contact ratio introduce stronger high-frequency components and transient impacts, increasing the vibration amplitude by 13.20% to 2.83 μm and the Poincaré section displacement.

To synthesize this influence, Fig. 15 compares the vibration amplitudes with and without meshing impact across all tested pressure angles. Two key insights are revealed: 1. The vibration amplitude follows a non-monotonic trend, reaching its minimum within the 30°–35° range, confirming it as the optimal window for dynamic stability. 2. While meshing impact consistently amplifies vibration, this amplification is weakest within the same optimal range, indicating the best trade-off between inherent stiffness and impact resistance. Overall, the driving-side pressure angle has a dual effect: moderate increases enhance stiffness and suppress low-frequency vibration, whereas excessively large angles amplify stiffness fluctuations and impacts, exciting high-frequency vibration. Fig. 15 provides a clear visual summary of this influence and the optimal range.

5. Conclusions

1. Based on the dynamic modeling theory of symmetric helical gears, a nonlinear dynamic model of asymmetric helical gears incorporating time-varying meshing stiffness and meshing impact excitations was established. The corresponding equations of motion were derived, and the time histories, phase portraits, and Poincaré maps were obtained through numerical simulations.

2. Comparative analysis between asymmetric and symmetric helical gears reveals that asymmetric helical gears exhibit higher average meshing stiffness, smaller vibration amplitudes, and more concentrated phase trajectories and Poincaré sections, indicating superior dynamic performance, which is consistent with previous research findings.

3. Time-varying meshing stiffness and meshing impact jointly govern the dynamic behavior of the system.

The system's vibration level exhibits a non-monotonic trend with increasing driving-side pressure angle, reaching its minimum within the 30°–35° range. Within this optimal window, the average stiffness and its fluctuation amplitude are well balanced, the meshing impact peaks are effectively suppressed, and the system exhibits the most stable response. In contrast, excessively small pressure angles lead to insufficient stiffness, whereas excessively large pressure angles intensify stiffness fluctuations and impacts, resulting in dispersed responses and reduced stability.

4. In summary, asymmetric helical gears maintain superior stability even when both time-varying meshing stiffness and meshing impact are considered. An appropriate selection of the driving-side pressure angle can balance load-carrying capacity and dynamic stability, providing useful guidance for the design and optimization of high-performance gear transmission systems.

Acknowledgments

This work was supported by the Guangxi Science and Technology Program (Nos. AD23026183 and AA24263072), and the National Natural Science Foundation of China Program (No. 52265006).

References

1. **Rajesh, S.; Marimuthu, P.; Babu, P. D.; Venkatraman, R.** 2022. Contact fatigue life estimation for asymmetric helical gear drives, International Journal of Fatigue 164: 107155. https://doi.org/10.1016/j.ijfatigue.2022.107155.
2. **Fu, X. Z.; Jin, Y. X.; Zhao, M. L.; Cao, F.** 2025. Asymmetric Helical Gears Bending Stress Calculation Formula, Mechanika 31(1): 44-51. https://doi.org/10.5755/j02.mech.39451.
3. **Litvin, F. L.; Lian, Q.; Kapelevich, A. L.** 2000. Asymmetric modified spur gear drives: reduction of noise, localization of contact, simulation of meshing and stress analysis, Computer Methods in Applied Mechanics and Engineering 188(1-3): 363-390. https://doi.org/10.1016/S0045-7825(99)00161-9.
4. **Kapelevich, A.** 2000. Geometry and design of involute spur gears with asymmetric teeth, Mechanism and Machine Theory 35(1): 117-130. https://doi.org/10.1016/S0094-114X(99)00002-6.
5. **Xiao, W. Q.; Li, W.; Han, J. Y.; Duan, M. N.** 2006. Contact analysis of asymmetric gears with double pressure angles, Journal of University of Science and Technology Beijing 2006(12): 1167-1173. https://doi.org/10.13374/j.issn1001-053x.2006.12.037.
6. **Xiao, W. Q.; Li, W.; Han, J. Y.; Tan, X. L.** 2006. Vibration analysis of asymmetric involute gears with double pressure angles, Chinese Mechanical Engineering 2006(6): 645-649.
7. **Xiao, W. Q.; Li, W.; Han, J. Y.** 2008. Analysis of the meshing mechanism of double pressure angle asymmetric tooth profile gears, Transactions of the Chinese Society for Agricultural Machinery, 39(5): 169-173.
8. **Demet, S. M.; Ersoyoğlu, A. S.** 2021. An analysis of the effect of pressure angle change on bending fatigue performance in asymmetrical spur gears, Proceedings of the Institution of Mechanical Engineers, Part L: Journal of Materials: Design and Applications 235(9): 2142-2150. https://doi.org/10.1177/14644207211026696.
9. **Demet, S. M.; Ersoyoğlu, A. S.** 2018. Fatigue fracture behaviour of asymmetric spur gear tooth under cyclic loading, Procedia Structural Integrity 13: 2030-2035. https://doi.org/10.1016/j.prostr.2018.12.213.
10. **Zhu, X. H.** 2014. Dynamics simulation of asymmetric involute gears based on ADAMS, Mechanical & Electrical Engineering Technology 43(8): 107-110.
11. **Marafona, J. D. M.; Marques, P. M. T.; Portron, S.; Martins, R. C.; Seabra, J.** 2023. Gear Mesh Stiffness and Dynamics: Influence of Stiffness Asymmetry, SSRN 4402142. https://dx.doi.org/10.2139/ssrn.4402142.
12. **Donmez, A.; Kahraman, A.** 2025. An investigation of dynamic behavior of electric vehicle gear trains, Journal of Computational and Nonlinear Dynamics 20(2): 021003. https://doi.org/10.1115/1.4067153.
13. **Mo, S.; Li, Y.; Wang, D.; Hu, X.; Cen, G.; Huang, Y.** 2023. An analytical method for the meshing characteristics of asymmetric helical gears with tooth modifications, Mechanism and Machine Theory 185: 105321. https://doi.org/10.1016/j.mechmachtheory.2023.105321.
14. **Mo, S.; Li, Y.; Luo, B.; Bao, H.; Cen, G.; Huang, Y.** 2022. Research on the meshing characteristics of asymmetric gears considering the tooth profile deviation, Mechanism and Machine Theory 175: 104926. https://doi.org/10.1016/j.mechmachtheory.2022.104926.
15. **Li, Y.; Dong, L.** 2025. Coupled dynamics and elastohydrodynamic lubrication model for asymmetric gears with numerical simulations, Journal of the Brazilian Society of Mechanical Sciences and Engineering 47(9): 1-18. https://doi.org/10.1007/s40430-025-05680-0.
16. **Yang, Y., Hu, J. H., Shi, Z. Q., Zhou, Q. H., Wu, J.** 2024. Precise calculation of meshing stiffness and analysis of tooth profile parameters for asymmetric gears, Mechanical Transmission, 48(3): 18-26. https://doi.org/10.16578/j.issn.1004.2539.2024.03.003.
17. **Chen, Q.; Yao, Z. G.; Wang, Y. D.; Wu, Y. M.** 2019. Dynamic characteristics of asymmetric involute gears considering time-varying stiffness and backlash, Journal of Mechanical Transmission 43(4): 15-20. https://doi.org/10.16578/j.issn.1004.2539.2019.04.004.
18. **Li, W.; Li, Z. Y.; Shi, H. Z.; Li, X. F.** 2023. Impact of phase configuration of a helical idler gear system on the vibration, Applied Acoustics 211: 109467. https://doi.org/10.1016/j.apacoust.2023.109467.
19. **Wang, C.** 2024. Influence of ingress impact considering the full-tooth meshing period on the dynamic behavior of helical gear systems, Mechanism and Machine Theory 201: 105756. https://doi.org/10.1016/j.mechmachtheory.2024.105756.
20. **Fu, X. Z.; Fang, Z. D.; Jia, C.; Peng, X. L.** 2019. Analysis of meshing stiffness and profile modification for vibration reduction of face gear drives, Vibration and Shock 38(5): 265-272. https://doi.org/10.13465/j.cnki.jvs.2019.05.038.
21. **Dong, H.; Liu, Z. Y.; Fang, Z. D.** 2019. Nonlinear dy-

namic characteristics analysis of high-speed gear transmission system based on LTCA, Composite Machine Tool & Automatic Machining Technology 2019(01): 17-20. https://doi.org/10.13462/j.cnki.mmtamt.2019.01.004.
22. **Tang, J. Y.; Liu, X.; Dai, J.** 2007. Study on off-line gear meshing impact based on ANSYS/LS-DYNA, Vibration and Shock 2007(9): 40-44. https://doi.org/10.13465/j.cnki.jvs.2007.09.021.
23. **Jia, C.; Yao, L. G.; Zhang, J.; Fang, Z. D.** 2020. Calculation of engagement impact for profile-modified involute helical gears, Journal of Xi'an Jiaotong University 2020: 5458-5465.
24. **Dong, J.; Tang, J.; Hu, Z.** 2021. Dynamic characteristics of the face gear transmission system based on a rotor-shaft-bearing model with multiple nodes, International Journal of Non-Linear Mechanics 137: 103825. https://doi.org/10.1016/j.ijnonlinmec.2021.103825.
25. **Wang, J.; Wang, H.; Guo, L.** 2017. Analysis of nonlinear dynamics and chaos control in gear transmission system with stochastic perturbation, Mechanika 23(2): 236-246. https://doi.org/10.5755/j01.mech.23.2.13576.
26. **Feng, M.; Ma, H.; Li, Z.; Wang, Q.; Wen, B.** 2018. An improved analytical method for calculating time-varying mesh stiffness of helical gears, Meccanica 53(4): 1131-1145. https://doi.org/10.1007/s11012-017-0746-6.

X. Z. Fu, J. S. Man, J. Zou, S. P. Li

INFLUENCE OF PRESSURE ANGLE ON THE DYNAMIC CHARACTERISTICS OF ASYMMETRIC HELICAL GEAR TRANSMISSIONS

S u m m a r y

To address the lack of research on the dynamic characteristics of asymmetric helical gears, this study systematically investigates their time-varying meshing stiffness and meshing impact characteristics based on the lumped-parameter method and nonlinear dynamic theory. An eight-degree-of-freedom dimensionless dynamic model is developed. Using the pressure angle on the driving side as the main variable, the dynamic characteristics of asymmetric and symmetric helical gears are compared, and the effects of different pressure angles on time-varying meshing stiffness, time histories, phase portraits, and Poincaré maps are analyzed. The results show that the asymmetric helical gear exhibits higher average meshing stiffness, smaller vibration amplitudes, and smoother responses than the symmetric gear. Within a driving-side pressure angle range of 30 to 35 degrees, the system achieves the best stability and periodicity, and the meshing impact amplitude is effectively suppressed. However, excessively small or large pressure angles lead to reduced system stability. This work clarifies the dynamic behavior of asymmetric helical gears and provides a theoretical basis for parameter design and high-performance transmission optimization.

Keywords: asymmetric helical gears, time-varying meshing stiffness, meshing impact, dynamic characteristics.

Received October 11, 2025
Accepted February 20, 2026